JACS
JOURNAL OF THE AMERICAN CHEMICAL SOCIETY
pubs.acs.org/JACS
Article

Increasing Iridium Oxide Activity for the Oxygen Evolution Reaction with Hafnium Modification

Fang Zhao,[¶] Bo Wen,[¶] Wenhan Niu, Zhu Chen, Chao Yan, Annabella Selloni, Christopher G. Tully, Xiaofang Yang,* and Bruce E. Koel*

Cite This: J. Am. Chem. Soc. 2021, 143, 15616−15623

ABSTRACT: Synthesis and implementation of highly active, stable, and affordable electrocatalysts for the oxygen evolution reaction (OER) is a major challenge in developing energy efficient and economically viable energy conversion devices such as electrolyzers, rechargeable metal-air batteries, and regenerative fuel cells. The current benchmark electrocatalyst for OER is based on iridium oxide (IrO_x) due to its superior performance and excellent stability. However, large scale applications using IrO_x are impractical due to its low abundance and high cost. Herein, we report a highly active hafnium-modified iridium oxide ($IrHf_xO_y$) electrocatalyst for OER. The $IrHf_xO_y$ electrocatalyst demonstrated ten times higher activity in alkaline conditions (pH = 11) and four times higher activity in acid conditions (pH = 1) than a IrO_x electrocatalyst. The highest intrinsic mass activity of the $IrHf_xO_y$ catalyst in acid conditions was calculated as 6950 A g_{IrOx}^{-1} at an overpotential (η) of 0.3 V. Combined studies utilizing operando surface enhanced Raman spectroscopy (SERS) and DFT calculations revealed that the active sites for OER are the Ir−O species for both IrO_x and $IrHf_xO_y$ catalysts. The presence of Hf sites leads to more negative charge states on nearby O sites, shortening of the bond lengths of Ir−O, and lowers free energies for OER intermediates that accelerate the OER process.

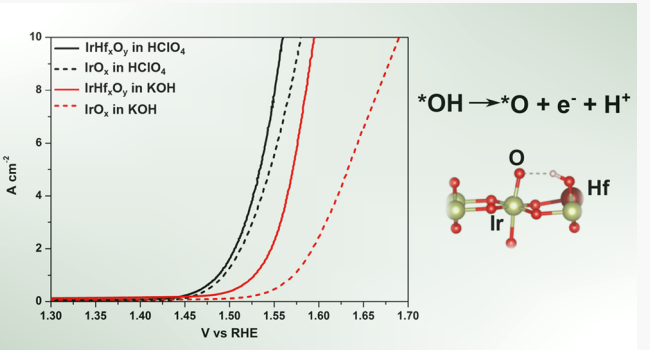

INTRODUCTION

The oxygen evolution reaction (OER) limits the performance of many electrochemical devices such as electrolyzers, rechargeable metal-air batteries, and regenerative fuel cells. Four electron transfer reactions involving multiple reaction intermediates create sluggish OER kinetics, which results in substantial overpotentials and causes a major loss in energy efficiency.[1] Thus, significant research effort has been aimed at improving and developing highly active, stable, and affordable OER catalysts.[1] Ru oxide and Ir oxide have demonstrated excellent catalytic activity and good electrical conductivity when implemented as OER catalysts under acidic and alkaline conditions.[1−5] Ir oxide-based catalysts have greater chemical stability in low pH conditions[4,6] compared to Ru oxide-based catalysts, which is highly desirable for long-term device operation. However, the low abundance and high cost of both Ir and Ru prevent their large-scale implementation as OER catalysts at the anode of many emergent energy conversion devices. Increasingly, research efforts have emphasized the synthesis and implementation of less expensive OER catalysts such as transition metal oxides (e.g., Co_3O_4)[7] and perovskite compounds[8−10] (e.g., (Pr, Ba)$Co_2O_{5+\delta}$). Hybridization of Ir with transition metals, such as oxides, nitrides, and hydroxides, has been successfully applied to construct Ir-based hybrids for upgrading OER with the advantage of the synergies of different components.[11−15] In particular, mixed metal (oxy)hydroxides comprised of combinations of Fe, Co, and Ni, which are intrinsically less efficient OER catalysts in their pure phases, have demonstrated excellent OER activity.[10,14−18] In bimetallic mixtures, these (oxy)hydroxide catalysts possess highly active reaction sites that enable optimal binding of reaction intermediates such as OH and OOH, which reduces the OER overpotential.[11−13,16−18] However, these transition metal-based oxide catalysts are only stable in neutral pH and alkaline conditions, and this makes them incompatible for use in devices such as PEM electrolyzers and regenerative fuel cells.

The high activity and superior stability of amorphous Ir oxide (IrO_x) in acidic conditions compared to other catalysts has resulted in substantial research on Ir oxide-based dimensionally stable anodes.[19−23] The formation of mixed

Received: April 1, 2021
Published: September 1, 2021

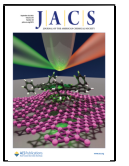

https://doi.org/10.1021/jacs.1c03473
J. Am. Chem. Soc. 2021, 143, 15616−15623

oxides with IrO_x via the addition of noble metals (e.g., Ru, Os, Rh)[24−26] and less expensive transition metals (e.g., Fe, Co, Ni)[14,15,27,28] is an attractive method for reducing the Ir loading and tuning the catalytic properties of IrO_x. The synergistic effects among Ir nanostructured alloy-based bifunctional catalysts have been developed to afford high activity in acidic media. The acid leaching process helps to remove excess Ni or Co to improve durability.[14,15] The nature of Ni or Co instability in acidic conditions remains as the major threat for Ir−Ni/Co alloy-based catalysts. Furthermore, the shaping and thermal control of the alloy nanostructure are also challenging, which profoundly regulate the arrangement of atoms of the active sites and surface configuration, and thereby influence the catalytic activity and stability. Likewise, several fundamental questions related to the high activity and stability of IrO_x for OER in acidic conditions remain unanswered, such as what the active sites are and how to stabilize IrO_x in acidic conditions.

In the work reported herein, we discovered a highly active, stable Ir oxide OER catalyst by hafnium (Hf) modification ($IrHf_xO_y$) under both acidic and alkaline conditions. Addressing the instability of transition metals (e.g., Fe, Ni, Co) in acidic conditions, we explore the early transition metals (Hf, Zr, Ti) as modifiers, which have excellent stability in strong acids. Ti, Zr, and Hf are early transition metals in group 3; Co and Ir are later transition metal elements in group 9. Previous studies suggested that the number of d-electrons in the transition metal ions of perovskite oxides is strongly correlated with OER activity,[29] with a general trend of lower activity for the early transitions metal oxides and higher activity for late transition metal oxides. More subtle models considering the number of valence electrons gives similar predictions of the reactivity trend for 3d transition metal oxides.[30,31] Thus, the bimetallic oxides we study are mixtures of lower and higher activity oxides. It has also been proposed that mixing early and late transition metals may lead to the selective tuning of the relative energies of important intermediates, (M−OH, M=O, and MOOH), leading to minimal OER reaction barriers.

In our study, the $IrHf_xO_y$ oxide layers (ca. 1 nm thick) were generated in situ under anodic polarization from a pristine bimetallic alloy having a bulk composition of $HfIr_3$. The $IrHf_xO_y$ thus formed demonstrated an order of magnitude increase in OER activity than a pure IrO_x thin film in 0.1 M KOH and a high mass specific activity of 6950 A g_{IrOx}^{-1} in 0.1 M $HClO_4$ at 0.3 V overpotential. Combined studies by operando surface enhanced Raman spectroscopy (SERS) and DFT calculations demonstrate that the active sites for OER are Ir−O species for both IrO_x and $IrHf_xO_y$ catalysts. The presence of Hf sites leads to more negative charge states on nearby O sites and shortens the bond lengths of Ir−O. The OER activity of $IrHf_xO_y$ catalysts is accelerated by the synergistic effects of structure and the lower free energies of OER intermediates. The remarkable OER activities of this $IrHf_xO_y$ catalyst in both acidic and alkaline conditions reported herein provide a new direction of mixing early tetravalent transition metals, such as Hf or Zr, with Ir or Ru for the development of cost-effective and high performance OER catalysts.

RESULTS AND DISSCUSSION

The zero-potential was determined by the onset of the hydrogen evolution reaction (HER) and hydrogen oxidation reaction (HOR) in the cyclic voltammetry (CV) scans using a polycrystalline Pt electrode immersed in a H_2-purged solution of 0.1 M KOH or 0.1 M $HClO_4$, as shown in Figure S1. OER polarization scans (Figure 1a) in O_2-purged 0.1 M KOH and 0.1 M $HClO_4$ solutions at 300 K were obtained by linearly scanning the electrode at 5 mV s^{-1} from 1.3 to 1.7 V vs reversible hydrogen electrode (RHE). As shown in Figure 1a, the OER onset potential(for current >0.2 mA) of the IrO_x catalyst in 0.1 M KOH was 1.53 V, or 0.30 V overpotential (η), which is comparable to the performance of Ir oxide

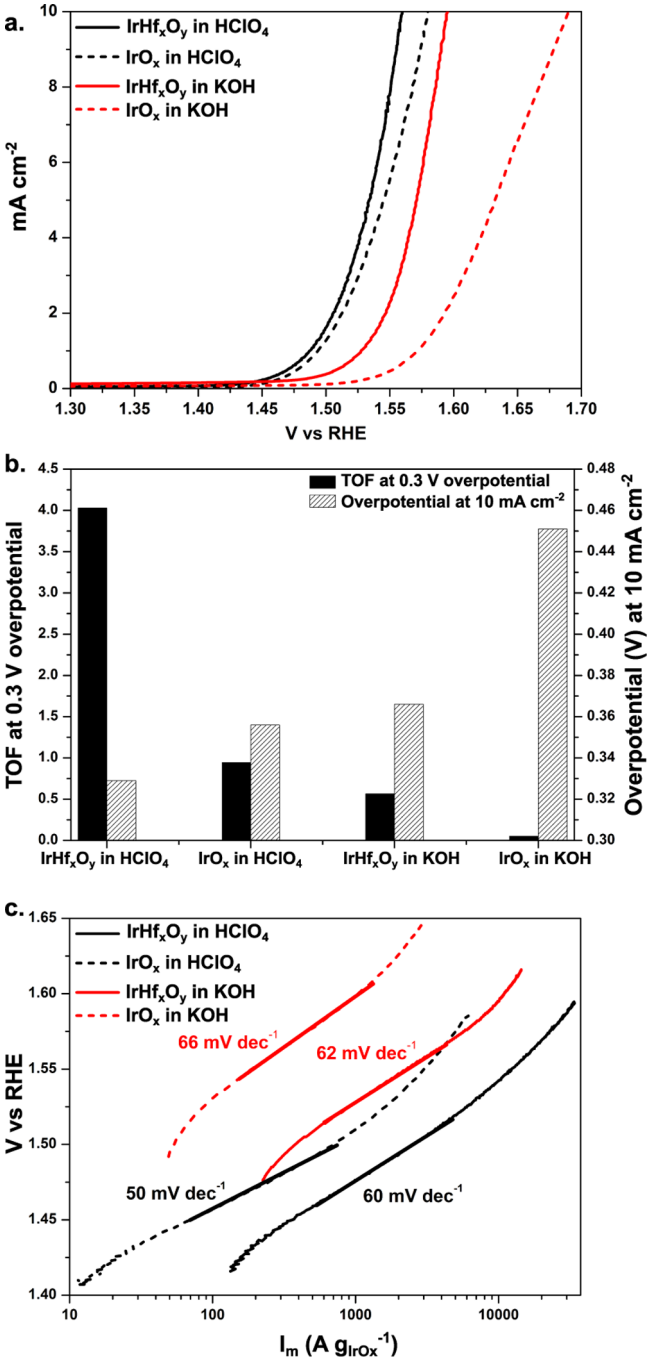

Figure 1. OER performance of IrO_x and $IrHf_xO_y$ films in O_2-saturated 0.1 M KOH and 0.1 M $HClO_4$ solutions at 300 K as measured by intrinsic catalytic activities. (a) OER polarization scans obtained at 5 mV s^{-1} with the RDE apparatus operated at 4500 rpm. (b) TOF at 0.3 V η and value of η required to reach 10 mA cm^{-2}. (c) Tafel plots comparing the mass specific activities and the corresponding Tafel slope values.

https://doi.org/10.1021/jacs.1c03473
J. Am. Chem. Soc. 2021, 143, 15616−15623

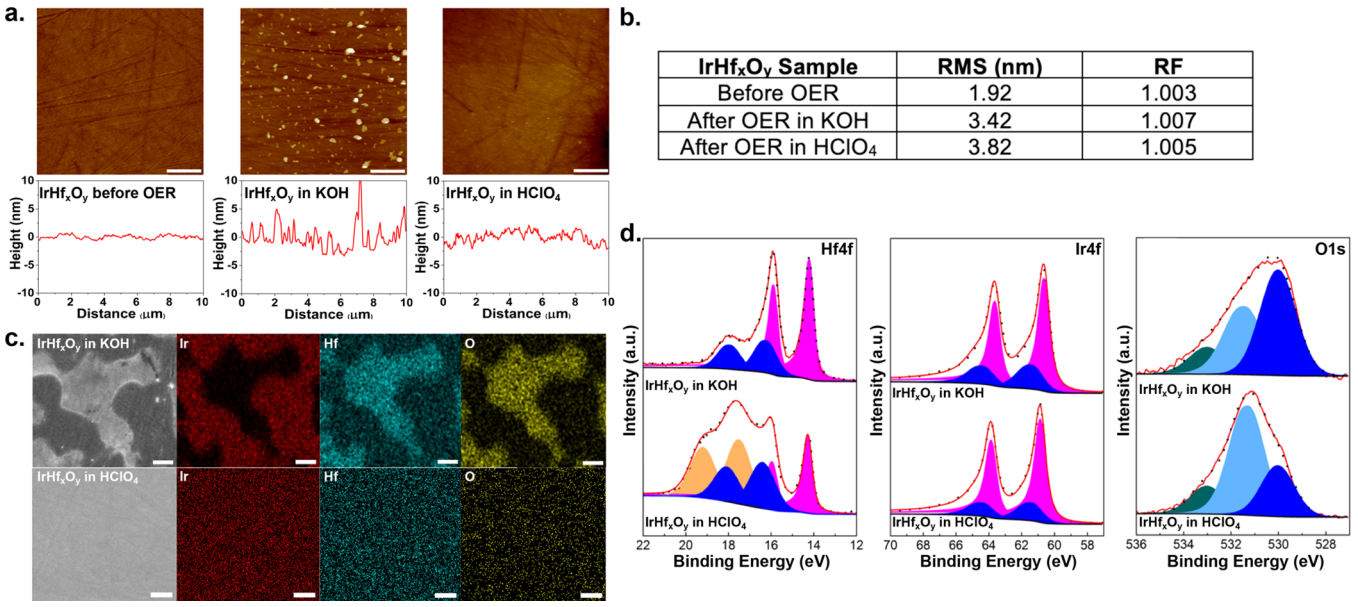

Figure 2. Characterization of the $IrHf_xO_y$ catalyst before and after cycling between 1.3 and 1.7 V vs RHE at 5 mV s^{-1} for 30 min for OER in 0.1 M KOH and 0.1 M $HClO_4$. (a) AFM images (top) and line scans (bottom). The line scans show the average height of all data points in the y direction of the AFM image. Scale bar: 2 μm. (b) Table summarizing the RMS roughness and RF values. (c) SEM images (left panels) and EDX elemental maps for Ir, Hf and O. Scale bar: 200 nm. (d) XPS spectra after OER in acidic and alkaline conditions for photoemission from Hf 4f (Hf^0: magenta; Hf^{2+}: blue; Hf^{4+}: orange), Ir 4f (Ir^0: magenta; Ir^{4+}: blue), and O 1s (O^{2-}: blue; OH^- or OOH^-: light blue; H_2O: green) core levels.

nanoparticles reported previously.[2] The onset potential for IrO_x in 0.1 M $HClO_4$ shifted to 1.45 V, or 0.22 V overpotential. The $IrHf_xO_y$ catalyst in 0.1 M KOH demonstrated significantly improved OER activity compared to the IrO_x catalyst, with the OER onset potential for $IrHf_xO_y$ reduced by 50 mV from that of IrO_x and with η at 10 mA cm^{-2} ($\eta_{10\ mA}$) at 0.37 V, 80 mV lower than that for IrO_x (Figure 1b). Likewise, in 0.1 M $HClO_4$, the $IrHf_xO_y$ catalyst demonstrated higher OER activity, and an onset potential reduced by 10 mV compared to the IrO_x catalyst. The intrinsic catalytic activity (normalized to the geometrical surface area) can be expressed as the turnover frequency (TOF), which is the number of molecules converted per site per second at the surface (Figure 1b). At η = 0.3 V, compared to IrO_x, $IrHf_xO_y$ had ten times higher OER activity in 0.1 M KOH and four times higher OER activity in 0.1 M $HClO_4$. An important parameter regarding precious metal- based catalysts is the mass activity, which is measured by the mass normalized current density (I_m [A g_{IrOx}^{-1}]). Details of the calculations of I_m and TOF are provided in the Supporting Information (SI), Figure S2 and Table S1. For $IrHf_xO_y$ in acid at η = 0.3 V, the value of I_m reaches 6950 A g_{IrOx}^{-1}, indicating the remarkable intrinsic activity of this catalyst. As shown in Figure 1c, the IrO_x and $IrHf_xO_y$ catalysts have similar Tafel slopes of 50−66 mV dec^{-1}. The Tafel slopes for the IrO_x catalyst are consistent with that reported previously for IrO_x.[32,33] Higher OER activity was observed in acidic compared to alkaline conditions for both IrO_x and $IrHf_xO_y$ catalysts in this study, which is consistent with prior studies that evaluated OER activity of Ir oxide nanoparticles and thin films at different pH values.[7,34,35]

The $IrHf_xO_y$ catalysts were characterized before and after electrochemical measurements to determine changes in catalyst morphology and composition. Atomic force microscopy (AFM) was used to measure changes in catalyst morphology and surface roughness caused by OER polarization. Figure 2a presents 10 × 10-μm^2 maps and 10-μm line scans for $IrHf_xO_y$ catalyst before and after OER reactions. To accurately report the intrinsic activity of an OER catalyst, the activity should be normalized to the true surface area, which depends on the surface roughness and the micro/nano structure. Values for the root-mean-square (RMS) roughness and surface roughness factor (RF) are given in Figure 2b. The RF is defined as the film surface area normalized to geometric area. The Hf-modified Ir surface prepared by polishing was quite flat, with an RMS roughness of 1.92 nm. After OER reaction in 0.1 M KOH, the $IrHf_xO_y$ surface exhibited some surface features and had an RMS roughness of 3.42 nm, whereas the surface after OER reaction in 0.1 M $HClO_4$ was rougher with an RMS roughness of 3.82 nm but without the small features. Although there were changes in the RMS values, the catalyst surfaces after OER reaction were notably nearly as flat as the "as polished" samples and have comparable RF values. These results from AFM measurements were applied to normalize the electrochemical activity to the true catalyst surface area. Analysis by scanning electron microscopy (SEM) and energy-dispersive X-ray spectroscopy (EDX), as shown in Figure 2c, indicated that after OER reaction the small features formed under alkaline conditions and observed in AFM and SEM were composed of primarily Hf oxide and the other region was composed of a mixture of Ir oxide and Hf oxide. Under acid conditions, EDX mapping of the surface showed a uniform distribution of all the elements and no small features were observed in SEM. Images from SEM and AFM are in agreement. SEM and EDX mapping for the Hf-modified Ir catalyst before OER reactions are shown in Figure S3.

The oxides formed in situ by CV scanning between 1.3 and 1.7 V in 0.1 M KOH and 0.1 M $HClO_4$ were analyzed by X-ray photoelectron spectroscopy (XPS) to determine surface compositions, oxidation states, and oxide layer thicknesses of the IrO_x and $IrHf_xO_y$ catalysts. The samples after OER reaction were controlled at a potential of 1.7 V before removal from the electrochemical cell. XPS scans of $IrHf_xO_y$ after OER reactions

https://doi.org/10.1021/jacs.1c03473
J. Am. Chem. Soc. 2021, 143, 15616−15623

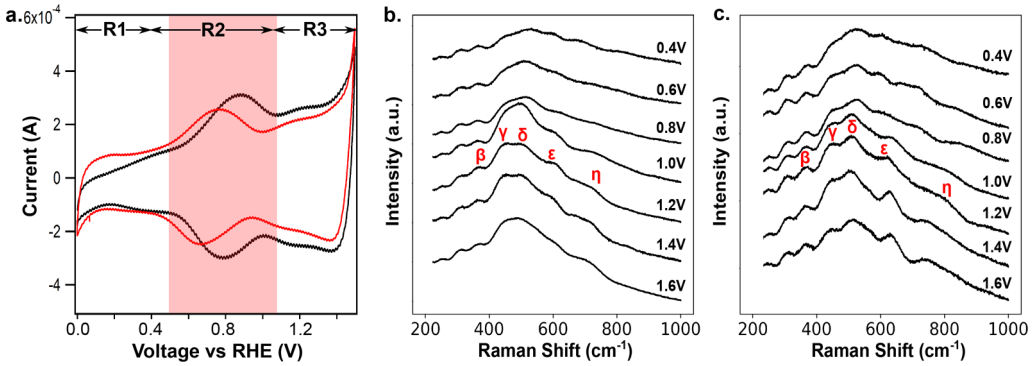

Figure 3. (a) CVs of IrO_x/Au (black) and $IrHf_xO_y$/Au (red) in 0.1 M $HClO_4$. Operando SERS from (b) IrO_x/Au film, and (c) $IrHf_xO_y$ film, in 0.1 M $HClO_4$. Peak assignments are adapted from Pavlovic et al.[36,37] for the Ir−O bending and stretching vibrations. The other peaks can be assigned to the Au substrate.[36]

are shown in Figure 2d. Other XPS spectra, such as of $IrHf_xO_y$, obtained after polishing and IrO_x after OER, are shown in Figure S4. The binding energies and peak intensities of all XPS peaks are tabulated in Table S2. The thickness of IrO_x and $IrHf_xO_y$ oxide layers can be estimated from calculations of the attenuation of the XPS signals from the metallic substrate and the calculation details are discussed in the SI. The thickness of the oxide layer was found to be 0.8 and 1.0 nm for $IrHf_xO_y$ and 1.5 Figure 2d shows Hf, Ir, and O XPS spectra for the $IrHf_xO_y$ catalyst after OER reactions. In 0.1 M KOH, 22% of the Hf signal Table S3 was due to Hf^{2+}. However, in 0.1 M $HClO_4$, 37% of the Hf signal was from Hf that underwent complete oxidation to Hf^{4+} and 27% was from Hf^{2+}. In both alkaline and acidic conditions, Ir was oxidized to Ir^{4+}, which shows an Ir $4f_{7/2}$ XPS peak at 61.5 eV binding energy. From EDX results, we assume a uniform distribution of Hf and Ir in the majority of the surface oxide layer. From Ir and Hf XPS spectra, the atomic concentration of Hf in the oxide layer in Table S2 was calculated to be 18% and 32% after OER in 0.1 M KOH and 0.1 M $HClO_4$, respectively. Comparing these values to the bulk Hf concentration (25%) in the pristine Hf-modified Ir catalyst, there is apparently a loss of surface Hf after OER in 0.1 M KOH due to Hf dissolution into solution. A highly active Ir oxide catalyst has been reported that was formed on a $SrIrO_3$ thin film surface by leaching out Sr from the SrIr oxide to form anatase IrO_2 motifs.[22] Another study observed that Ir−Ni and Ir−Co nanowires after acid leaching showed improved mass activities and high durabilities.[14] The leaching of sacrificial metals results in an Ir-rich surface, which facilitates the formation of active IrO_x layers. In our study, the formation of such motifs and the dissolution of Hf observed using XPS, AFM and SEM analysis might be due to a leaching process that contributes to an Ir hydroxide-dominant surface during OER in 0.1 M KOH. However, after acidic OER reactions, XPS analysis indicated the surface Hf concentration did not experience a decrease. Therefore, we cannot explain the enhanced OER activity of $IrHf_xO_y$ in acid by the leaching of Hf as was possible under alkaline conditions. The O 1s XPS peaks at 530, 531.5, and 533 eV are assigned to oxide, hydroxide or oxyhydroxide (OH or OOH), and H_2O, respectively.[3] In alkaline conditions, the majority of the O 1s XPS peak is from oxide. However, a large OH peak appears after OER reaction in acid. This was also observed for the IrO_x catalyst (Figure S4c), indicating that Ir hydroxide ($Ir(OH)_4$) or oxyhydroxide ($IrO(OH)_2$) was preferentially formed in acidic OER conditions, while IrO_2 was preferentially formed in alkaline OER conditions. Since the OER activity of Ir oxides in acid conditions is about one order magnitude higher than that in alkaline conditions, the formation of hydroxide ($Ir(OH)_4$) or oxyhydroxide ($IrO(OH)_2$) is a likely important contribution for the enhanced activity in acid conditions.

To understand the formation and nature of active sites during acidic OER on the $IrHf_xO_y$ catalyst, operando SERS spectroscopy measurements were performed on Ir and Ir−Hf oxide thin film samples prepared by sputter deposition of Ir and Ir−Hf (composition of 3:1 for Ir:Hf), respectively, with a 10 nm film thickness on roughed Au foils (CVs of Au foils roughening shown in Figure S5). After electrochemical cycling (0.2−1.5 V, scan rate 0.01 V s^{-1}) for 200 cycles in 0.1 M $HClO_4$, the IrO_x and $IrHf_xO_y$ catalysts were formed and measured by operando SERS under acidic conditions. Stability measurements of the catalysts were carried on the 10 nm thin film samples deposited by the sputter deposition on the roughened Au foils. The activity of both catalysts decreased by 3% after 6 h scan (as shown in Figure S5), demonstrating that both of IrO_x and $IrHf_xO_y$ display the comparable stability. Figure 3a shows stable CVs of IrO_x and $IrHf_xO_y$ in 0.1 M $HClO_4$ between 0 and 1.5 V. Three regions (R) can be identified, **R1** (E < 0.5 V), **R2** (0.5 < E < 1.05 V), and **R3** (1.05 < E < 1.5 V). **R1** corresponds to an Ir oxide rich in Ir^{3+}. In the forward scan, **R2** is the oxidation of Ir^{3+} to Ir^{4+}, and **R3** is the oxidation of Ir^{4+} to higher oxidation states.[36−39] Thus, two Ir redox couples can be identified for each catalyst: (i) Ir^{3+}/Ir^{4+} at 0.9/0.79 V and Ir^{4+} /Ir^{5+} at 1.22/1.15 V for the IrO_x catalyst; (ii) Ir^{3+}/Ir^{4+} at 0.77/0.66 V and Ir^{4+} /Ir^{5+} at 1.16/1.09 V for the $IrHf_xO_y$ catalyst. Mixing with Hf causes the potentials of the redox couples to negatively shift by 0.13 V for Ir^{3+}/Ir^{4+} and by 0.06 V for Ir^{4+}/Ir^{5+}.

This negative shift has been observed previously for the highly active $IrNiO_x$ catalyst.[40] It was proposed that oxidation of Ir^{4+} to Ir^{5+} is correlated with the start of OER activity (the onset potential). The negative shift of the oxidation potential for the Ir^{4+}/Ir^{5+} redox couple in $IrHf_xO_y$ agrees with the lowering of the OER onset potential (by 10 mV as shown in Figure 1).

During operando Raman measurements, the sample was controlled at a potential of 0.4, 0.6, 0.8, 1.0, 1.2, 1.4, and 1.6 V (vs RHE) for 60 s and then Raman spectra were recorded over the range of 200−1000 cm^{-1}. The Raman spectra obtained from IrO_x and $IrHf_xO_y$ thin films are shown in Figure 3b,c. Compared to the narrow Raman peaks for highly crystalline IrO_2,[40] the Raman peaks are broad for the IrO_x and $IrHf_xO_y$

https://doi.org/10.1021/jacs.1c03473
J. Am. Chem. Soc. 2021, 143, 15616−15623

catalysts generated in situ in these experiments, indicating poor crystallinity of these oxide catalysts. In addition, the peak positions are strongly dependent on the applied potentials on the sample, which cause different oxidation states of the Ir species. Peaks at 237 and 316 cm^{-1} originate from the Au surface.[36] The peak assignments for both IrO_x and $IrHf_xO_y$ are summarized and compared to values previously reported for IrO_x in Table 1.[36,37]

Table 1. Peaks in Raman Spectra of IrO_x and $IrHf_xO_y$ in 0.1 M $HClO_4$ at 1.2 V vs RHE

		Raman shift (cm^{-1})		
Peak label	Vibration	IrO_x	$IrHf_xO_y$	IrO_x[36,37]
β	Ir−O bend	360	360	358
γ	Ir−O stretch	433	442	445
δ	Ir−O stretch	500	515	482
ε	Ir−O or Hf−O stretch	600	637	602
η	Ir−O stretch (out-of-plane)	724	745	706

An edge-sharing tetrameric cluster composed of octahedral $[IrO_6]_n$ units was applied for describing the anodically formed Ir oxides in previous studies.[36,37] These octahedra are connected to each other via μ-oxo type linkages. This distorted Ir−O species has been proposed to be the OER active sites and was characterized by Raman spectroscopy.[37] The bending modes of Ir−O species in the basal plane have Raman peaks at 300−400 cm^{-1}. The stretching modes of Ir−O species in the basal plane have Raman peaks between 400−700 cm^{-1}. Raman peak above 700 cm^{-1} have been assigned to Ir−O out-of-plane stretching modes of a square pyramidal structure. As shown in Figure 3b,c and Table 1, in the potential region **R2** the Ir oxide undergoes oxidation from Ir^{3+} to Ir^{4+}, with decreased intensity for Ir−O δ stretching vibrations associated with Ir^{3+} and increased Ir−O γ stretching vibrations associated with Ir^{4+}. As the potential increases to 1.0 V, two new peaks appear at $\varepsilon \sim$ 600 cm^{-1} and $\eta \sim$ 730 cm^{-1}. Increasing the potential further from 1.4 and 1.6 V, no new potential-dependent peaks appear, indicating that the main structure of the Ir−O is stable in this potential range. Examination of the ε and η peaks reveals that they shift slightly to lower wavenumbers as the potential increases from 1.0 to 1.6 V. This shift has been observed before and was explained as due to the weakening of Ir−O bonds caused by increasing the applied potential.[37] At potentials of 1.0−1.6 V, the ε peak near 600 cm^{-1} appears in both catalysts, with the ε peak in $IrHf_xO_y$ more recognizable. It can be assigned to the Hf−O or Ir−O stretching mode. The comparison of the Raman peaks of IrO_x and $IrHf_xO_y$ (Table 1) reveals that peaks associated with Ir−O stretching modes shift to higher wavenumbers in the $IrHf_xO_y$ catalyst, indicating a shorter Ir−O bond length d, assuming that the stretching frequency ν (cm^{-1}) is related to d by an exponential function with the form of $\nu = 25823 \exp(-1.902d)$.[41,42] The shifts of these Raman peaks confirm the strong electronic influence on Ir induced by the presence of Hf and this may be associated with the higher OER activity of $IrHf_xO_y$ compared to IrO_x.

To study the effect of the Hf modification on the structure and reactivity of IrO_x, we performed DFT calculations on periodic slab models of the (110) surface of pristine rutile IrO_2 and Hf-doped $Hf_{0.25}Ir_{0.75}O_2$ crystals (computational details are give in the SI). We note that a similar model was used to describe the reactivity of IrO_x in a recent study.[39] As shown in Figure 4, rutile (110) surfaces expose alternate rows of 5-coordinated Ir/Hf and 2-coordinated O sites along the $[1\bar{1}0]$ direction. The $Hf_{0.25}Ir_{0.75}O_2$ slab was generated by regularly distributing the Hf dopants into each layer whereas on the surface the Hf positions were adjusted to realize different types of water adsorption (i.e., under-coordinated metal) sites. The OER activities of three inequivalent Ir sites were compared: **I** near Hf; **II** between Ir; and **III** between Hf. For simplicity, free energies were approximated by total energies for this comparison. The effect of Hf modification was analyzed on the Mulliken charges of the metal and oxygen sites of the bare IrO_2(110) surface. As shown in Figure 4, the changes of Mulliken charges are very small for the Ir atoms, whereas significantly more negative charges are observed on the O atoms bonded to one (or more) Hf atom(s) on the doped surface.

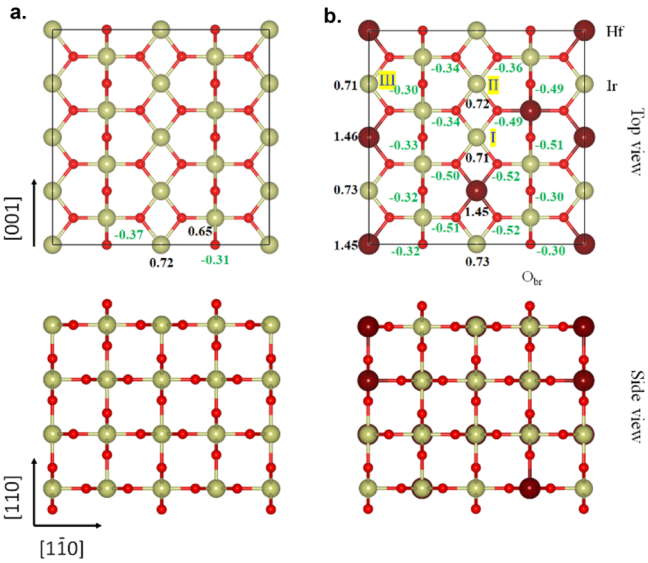

Figure 4. Top (upper row) and side (lower row) views of the rutile (110) slab models investigated in this work: (a) pristine IrO_2, and (b) Hf-doped $Hf_{0.25}Ir_{0.75}O_2$. The slabs include four oxide layers and a (4 × 2) surface supercell. Numerical values represent Mulliken charges of relevant Ir/Hf in black color and O sites in green color. In (b), three inequivalent Ir sites are labeled as **I** near Hf; **II** between Ir; and **III** between Hf. The red, gold and wine-colored spheres represent O, Ir and Hf atoms, respectively.

The adsorbate evolution mechanism (AEM) is widely accepted for the OER, and it was found to be consistent with numerous experimental investigations.[39,43] In this mechanism, oxygen molecules only come from the water molecules in the electrolyte and their formation occurs via four proton-coupled electron transfer (PCET) steps (Figure 5a). In step 1, adsorbed *OH species are formed by H_2O dissociative adsorption at an Ir site, followed by formation of *O species upon proton release (step 2). Next, nucleophilic attack of an H_2O molecule on *O leads to the formation of a hydroperoxide intermediate *OOH (step 3), which subsequently deprotonates to release an O_2 molecule and regenerate the Ir site (step 4).[43] Formation of *O or *OOH has been proposed to be rate determining in several OER studies on iridium oxides,[21,39,44−46] with a corresponding Tafel slope of 30−40 mV/dec predicted by microkinetic analysis.[33,47] A rate-determining step involving a chemical reaction (rather than a PCET) is predicted for a Tafel slope of ~60 mV/dec (Figure 1c), but there is no consensus on the nature of the reaction.[33,47] Given this uncertainty, we focus on the energetics

https://doi.org/10.1021/jacs.1c03473
J. Am. Chem. Soc. 2021, 143, 15616−15623

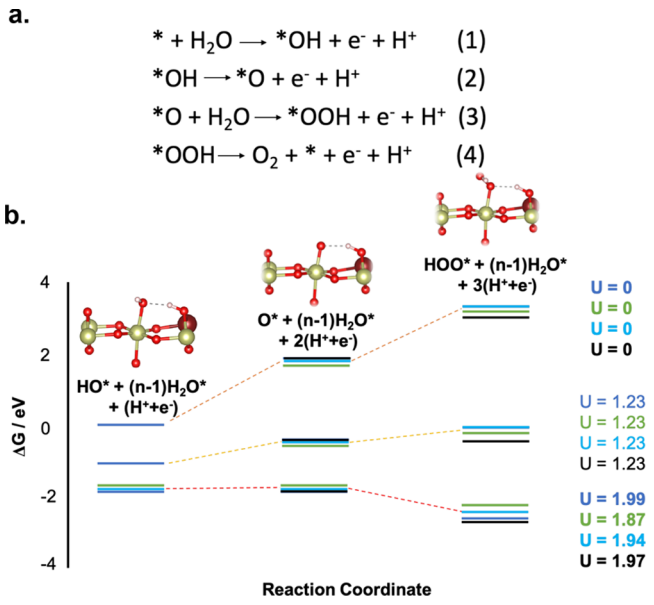

Figure 5. (a) The four steps of the adsorbate evolution mechanism (AEM) for OER in an acidic environment. (b) Computed free energies of OER intermediates on pristine rutile IrO_2 (black) and Hf-doped $Hf_{0.25}Ir_{0.75}O_2$ (110) surfaces for different values of the applied potential U and pH = 0. On the doped surface, sites I (green), II (blue) and III (cyan) are considered. Three Ir sites are labeled in Figure 4 as **I** near Hf; **II** between Ir; and **III** between Hf. In all cases, the energy zero refers to the surface covered by a full monolayer of dissociated water. The three model insets present the computed OER intermediates on site I of the Hf-doped surface (the full model is shown in Figure S7).

of step 2 and step 3 to estimate the *relative* OER activities of different sites (Figure 5b).

We considered surfaces covered by one monolayer of dissociated water, which is the most favorable water adsorption configuration at full coverage. In this configuration, terminal OH species are present at all the metal 5c sites of the bare surface while the dissociated protons are adsorbed at the surface 2c oxygen sites. The computed average adsorption energies for the monolayer are −1.92 and −1.70 eV/H_2O on the pristine and doped surfaces, respectively. We then calculated the free energy changes associated with the formation of the *O and *OOH radical intermediates of the OER according to

$$HO^* + (n-1)H_2O^* + O_{br}H \rightarrow O^* + (H^+ + e^-) + (n-1)H_2O^* + O_{br}H \quad (1)$$

$$O^* + (n-1)H_2O^* + O_{br}H + H_2O \rightarrow HOO^* + (H^+ + e^-) + (n-1)H_2O^* + O_{br}H \quad (2)$$

where X^* denotes an adsorbed X species. The activities of four different Ir sites were examined (Figure 5b, Table S4, and Figure S7), and in all the cases, the step with highest free energy cost was the formation of *O (Step 2), as found in other studies.[45] The activity of a surface Hf site was also studied. However, our results show that *O on Hf is highly unstable and spontaneously captures a proton from a neighboring $O_{br}H$. Therefore, we did not further consider Hf as a possible OER active site in our study.

On the basis of our results, site I, second neighbor of two surface Hf atoms, is the most favorable one: its overpotential of 0.64 V is 0.1 V lower than that of pristine IrO_2 and thus leads to a lower thermodynamic barrier and faster OER kinetics. Moreover, the in-plane Ir−O bond lengths along the [1$\bar{1}$0] direction on the $Hf_{0.25}Ir_{0.75}O_2$ surface (1.94 Å −2.01 Å) are shorter than those on the IrO_2 surface (1.99 Å). This is consistent with the operando Raman shift in the Ir−O stretching modes to higher wavenumbers for $IrHf_xO_y$ compared to those observed for IrO_x.

In summary, the active sites of the OER are the Ir−O species, while the presence of Hf sites leads to more negative charge states on nearby O sites and shortens the Ir−O bond lengths. The synergistic effects of structure and free energy changes of the intermediates can accelerate the OER process.

CONCLUSION

We report here a highly active $IrHf_xO_y$ catalyst for OER, which was formed in situ at the surface of a $HfIr_3$ bimetallic alloy electrode by anodic polarization under acidic and alkaline conditions. The $IrHf_xO_y$ catalyst significantly outperforms the IrO_x catalyst, as indicated by a large decrease (80 mV) in the overpotential (η) for the onset of OER and a factor of 10 increase in the current density at η = 0.3 V under alkaline conditions. The dissolution of Hf and formation of special motifs may be responsible for this enhancement in OER activity under alkaline conditions. However, a unique composite surface generated in acidic conditions resulted in an $IrHf_xO_y$ catalyst that also greatly exceeds the performance of an IrO_x catalyst. Operando SERS measurements indicate that the active sites for OER are Ir−O species for both IrO_x and $IrHf_xO_y$, and the presence of Hf induces a shift in the Ir−O stretching modes to higher wavenumbers in the $IrHf_xO_y$ catalyst, indicating a shorter Ir−O bond length. This view is supported by DFT calculations on pristine and Hf-doped IrO_2 (110) surfaces, which indicate that the Ir−O species are as the active sites of OER, and higher charge states of O sites can be achieved by Hf modification. Additionally, the incorporation shortens the Ir−O bond lengths along the [1$\bar{1}$0] direction and lowers the free energies of OER intermediates. This discovery opens a new direction of modifications to achieve high performance OER catalysts by mixing early tetravalent transition metals, such as Hf or Zr, with Ir or Ru for the development of cost-effective and high performance OER catalysts.

ASSOCIATED CONTENT

Supporting Information

The Supporting Information is available free of charge at https://pubs.acs.org/doi/10.1021/jacs.1c03473.

Experimental details, calculation of the mass specific current density and turnover frequency, calculation of the surface composition of $IrHf_xO_y$ catalysts, determination of the thickness of IrO_x and $IrHf_xO_y$ films, determination of the zero-potential vs RHE, electroactivities of the IrO_2, SEM and EDX of Hf-modified Ir catalyst before OER reactions, XPS spectra of Ir and Hf-modified Ir catalysts, comparison of Ir-based catalysts' mass activity in acidic conditions, summary of XPS results, table of oxide layer's thickness, CVs of Au foil roughening, catalyst stability measurement, and DFT

https://doi.org/10.1021/jacs.1c03473
J. Am. Chem. Soc. 2021, 143, 15616−15623

calculated values of OER intermediates' formation free energies (PDF)

AUTHOR INFORMATION

Corresponding Authors

Bruce E. Koel − *Department of Chemical and Biological Engineering, Princeton University, New Jersey 08540, United States;* orcid.org/0000-0002-0032-4991; Email: bkoel@princeton.edu

Xiaofang Yang − *Department of Chemical and Biological Engineering, Princeton University, New Jersey 08540, United States;* Present Address: Princeton NuEnergy Inc., Bordentown, NJ 08505, United States.; Email: xiaofang_yang@pnecycle.com

Authors

Fang Zhao − *Department of Physics, Princeton University, New Jersey 08544, United States;* orcid.org/0000-0001-6710-5016

Bo Wen − *Department of Chemistry, Princeton University, New Jersey 08544, United States;* Present Address: School of Physics and Electronics, Henan University, Kaifeng 475001, China

Wenhan Niu − *Department of Chemical and Biological Engineering, Princeton University, New Jersey 08540, United States;* orcid.org/0000-0003-1494-4435

Zhu Chen − *Department of Chemical and Biological Engineering, Princeton University, New Jersey 08540, United States;* Present Address: Department of Chemistry, University of Toronto, Toronto, ON M5S 3H6, Canada.; orcid.org/0000-0001-5889-5415

Chao Yan − *Department of Mechanical and Aerospace Engineering, Princeton University, New Jersey 08540, United States;* orcid.org/0000-0002-2415-6080

Annabella Selloni − *Department of Chemistry, Princeton University, New Jersey 08544, United States;* orcid.org/0000-0001-5896-3158

Christopher G. Tully − *Department of Physics, Princeton University, New Jersey 08544, United States*

Complete contact information is available at: https://pubs.acs.org/10.1021/jacs.1c03473

Author Contributions

¶F.Z. and B.W. contributed equally. All authors contributed to the analysis of the results and commented on the manuscript.

Notes

The authors declare no competing financial interest.

ACKNOWLEDGMENTS

This material is based upon work supported by the National Science Foundation under Grant No. CHE-1800376. F.Z. and C.G.T acknowledge financial support by the Simons Foundation (#377485) and John Templeton Foundation (#58851). B.W. and A.S. acknowledge the support of DOE BES, CSGB Division under Award DESC0007347. We used resources of the National Energy Research Scientific Computing Center (DoE No. DE-AC02-05cH11231) and the TIGRESS high-performance computer center at Princeton University. We also acknowledge the use of Princeton's Imaging and Analysis Center, which is partially supported through the Princeton Center for Complex Materials (PCCM), a National Science Foundation (NSF)-MRSEC program (DMR-2011750).

REFERENCES

(1) Wang, Z. L.; Xu, D.; Xu, J. J.; Zhang, X. B. Oxygen electrocatalysts in metal-air batteries: from aqueous to nonaqueous electrolytes. *Chem. Soc. Rev.* **2014**, *43*, 7746−7786.

(2) Kötz, R.; Stucki, S.; Scherson, D.; Kolb, D. In-situ identification of RuO_4 as the corrosion product during oxygen evolution on ruthenium in acid media. *J. Electroanal. Chem. Interfacial Electrochem.* **1984**, *172*, 211−219.

(3) Lee, Y.; Suntivich, J.; May, K. J. Synthesis and activities of rutile IrO_2 and RuO_2 nanoparticles for oxygen evolution in acid and alkaline solutions. *J. Phys. Chem. Lett.* **2012**, *3*, 399−404.

(4) Shan, J.; Guo, C.; Zhu, Y.; Chen, S.; Song, L.; Jaroniec, M.; Zheng, Y.; Qian, S. Z. Charge-redistribution-enhanced nanocrystalline Ru@IrO_x electrocatalysts for oxygen evolution in acidic media. *Chem.* **2019**, *5*, 445−459.

(5) Over, H. Fundamental studies of planar single-crystalline oxide model electrodes (RuO_2, IrO_2) for acidic water splitting. *ACS Catal.* **2021**, *11*, 8848−8871.

(6) Reier, T.; Oezaslan, M.; Strasser, P. Electrocatalytic oxygen evolution reaction (OER) on Ru, Ir, and Pt catalysts: a comparative study of nanoparticles and bulk materials. *ACS Catal.* **2012**, *2*, 1765−1772.

(7) Cherevko, S.; Geiger, S.; Kasian, O. Oxygen and hydrogen evolution reactions on Ru, RuO_2, Ir, and IrO_2 thin film electrodes in acidic and alkaline electrolytes: a comparative study on activity and stability. *Catal. Today* **2016**, *262*, 170−180.

(8) Liang, Y.; Li, Y.; Wang, H. Co_3O_4 nanocrystals on graphene as a synergistic catalyst for oxygen reduction reaction. *Nat. Mater.* **2011**, *10*, 780−786.

(9) Grimaud, A.; May, K. J.; Carlton, C. E. Double perovskites as a family of highly active catalysts for oxygen evolution in alkaline solution. *Nat. Commun.* **2013**, *4*, 2439.

(10) Suntivich, J.; May, K. J.; Gasteiger, H. A. A perovskite oxide optimized for oxygen evolution catalysis from molecular orbital principles. *Science* **2011**, *334*, 1383−1385.

(11) Zhao, G.; Li, P.; Cheng, N.; Dou, S. X.; Sun, W. An Ir/$Ni(OH)_2$ heterostructured electrocatalyst for the oxygen evolution reaction: breaking the scaling relation, stabilizing iridium (V), and beyond. *Adv. Mater.* **2020**, *32*, 2000872.

(12) Xing, Y.; Ku, J.; Fu, W.; Wang, L.; Chen, H. Inductive effect between atomically dispersed iridium and transiton-metal hydroxide nanosheets enables highly efficient oxygen evolution reaction. *Chem. Eng. J.* **2020**, *395*, 125149.

(13) Zhang, Y.; Wu, C.; Jiang, H.; Lin, Y.; Liu, H.; He, Q.; Chen, S.; Duan, T.; Song, L. Atomic iridium incorporated in cobalt hydroxide for efficient oxygen evolution catalysis in neutral electrolyte. *Adv. Mater.* **2018**, *30*, 1707522.

(14) Alia, S. M.; Shulda, S.; Ngo, C.; Pylypenko, S.; Pivovar, B. S. Iridum-based nanowires as highly active, oxygen evolution reaction electrocatalysts. *ACS Catal.* **2018**, *8*, 2111−2120.

(15) Godinez-Salomo, F.; Albiter, L.; Alia, S. M.; Pivovar, B. S.; Camacho-Forero, L. E.; Balbuena, P. B.; Mendoza-Cruz, R.; Arellano-Jimenez, M. J.; Rhodes, C. P. Self-supported hydrous iridium-nickel oxide two-dimensional nanoframes for high activity evolution electrocatalysts. *ACS Catal.* **2018**, *8*, 10498−10520.

(16) Liang, H.; Meng, F.; Cabán-Acevedo, M. Hydrothermal continuous flow synthesis and exfoliation of NiCo layered double hydroxide nanosheets for enhanced oxygen evolution catalysis. *Nano Lett.* **2015**, *15*, 1421−1427.

(17) Li, Y.; Hasin, P.; Wu, Y. $Ni_xCo_{3-x}O_4$ nanowire arrays for electrocatalytic oxygen evolution. *Adv. Mater.* **2010**, *22*, 1926−1929.

(18) Chung, D. Y.; Lopes, P. P.; Martins, P. F. B. D.; He, H.; Kawaguchi, T.; Zapol, P.; You, H.; Tripkovic, D.; Strmcnik, D.; Zhu, Y.; Seifert, S.; Lee, S.; Stamenkovic, V. R.; Markovic, N. M. Dynamic stability of active sites in hydro(oxy)oxides for the oxygen evolution reaction. *Nat. Energy* **2020**, *5*, 222−230.

(19) Oh, H. S.; Nong, H. N.; Reier, T.; Gliech, M.; Strasser, P. Oxide-supported Ir nanodendrites with high activity and surability for the oxygen evolution reaction in acid PEM water electrolyzers. *Chem. Sci.* **2015**, *6*, 3321.
(20) Ohno, H.; Nohara, S.; Kakinuma, K.; Uchida, M.; Miyake, A.; Deki, S.; Uchida, H. Remarkable mass activities for the oxygen evolution reaction at iridium oxide nanocatalysts dispersed on tin oxides for polymer electrolyte membrane water electrolysis. *J. Electrochem. Soc.* **2017**, *164*, F944.
(21) Kuo, D. Y.; Kawasaki, J. K.; Nelson, J. N. Influence of Surface Adsorption on the Oxygen Evolution Reaction on IrO_2(110). *J. Am. Chem. Soc.* **2017**, *139*, 3473−3479.
(22) Seitz, L. C.; Dickens, C. F.; Nishio, K. A highly active and stable IrOx/SrIrO3 catalyst for the oxygen evolution reaction. *Science* **2016**, *353*, 1011−1014.
(23) Antolini, E. Iridium as catalyst and cocatalyst for oxygen evolution/reduction in acidic polymer electrolyte membrane electrolyzers and fuel cells. *ACS Catal.* **2014**, *4*, 1426−1440.
(24) Din, M. A. U.; Irfan, S.; Ullah Dar, S.; Rizwan, S. Synthesis of 3D IrRuMn sphere as a superior oxygen evolution electrocatalyst in acidic environment. *Chem. - Eur. J.* **2020**, *26*, 5663.
(25) Kim, Y. T.; Lopes, P. P.; Park, S. A.; Lee, A. Y.; Lim, J.; Lee, H.; Bark, S.; Jung, Y.; Danilovic, N.; Stamenkovic, V.; Erlebacher, J.; Snyder, J.; Markovic, N. M. Balancing activity, stability and conductivity of nanoporous core-shell iridium/iridium oxide oxygen evolution catalysts. *Nat. Commun.* **2017**, *8*, 1449.
(26) Guo, H.; Fang, Z.; Li, H.; Fernandez, D.; Henkelman, G.; Humphrey, S. M.; Yu, G. Rational design of rhodium-iridium alloy nanoparticles as highly active catalysts for acidic oxygen evolution. *ACS Nano* **2019**, *13*, 13225−13234.
(27) Zhao, Y.; Luo, M.; Chu, S.; Peng, M.; Liu, B.; Wu, Q.; Liu, P.; de Groot, F. M. F.; Tan, Y. 3D nanoporous iridium-based alloy microwires for efficient oxygen evolution in acidic media. *Nano Energy* **2019**, *59*, 146−153.
(28) Wang, Y.; Zhang, L.; Yin, K.; Zhang, J.; Gao, H.; Liu, N.; Peng, Z.; Zhang, Z. Nanoporous iridium-based alloy nanowires as highly efficient electrocatalysts toward acidic oxygen evolution reaction. *ACS Appl. Mater. Interfaces* **2019**, *11*, 39728−39736.
(29) Bockris, J.; Otagawa, T. The electrocatalysis of oxygen evolution on perovskites. *J. Electrochem. Soc.* **1984**, *131*, 290−302.
(30) Busch, M.; Ahlberg, E.; Panas, I. Hydroxide oxidation and peroxide formation at embedded binuclear transition metal sites; TM= Cr, Mn, Fe, Co. *Phys. Chem. Chem. Phys.* **2011**, *13*, 15062−15068.
(31) Busch, M.; Ahlberg, E.; Panas, I. Validation of binuclear descriptor for mixed transition metal oxide supported electrocatalytic water oxidation. *Catal. Today* **2013**, *202*, 114−119.
(32) Oh, H.; Nong, H. N.; Reier, T.; Bergmann, A.; Gliech, M.; de Araujo, J. F.; Willinger, E.; Schlogl, R.; Teschner, D.; Strasser, P. Electrochemical catalyst-support effects and their satbilizing role for IrOx Nanoparticle catalysts during the oxygen evolution reaction. *J. Am. Chem. Soc.* **2016**, *138*, 12552−12563.
(33) Hu, J. M.; Zhang, J. Q.; Cao, C. N. Oxygen evolution reaction on IrO_2 based DSA® type electrodes: kinetics analysis of Tafel lines and EIS. *Int. J. Hydrogen Energy* **2004**, *29*, 791−797.
(34) Giordano, L.; Han, B.; Risch, M. PH dependence of OER activity of oxides: current and future perspectives. *Catal. Today* **2016**, *262*, 2−10.
(35) Lee, Y.; Suntivich, J.; May, K. J. Synthesis and activities of rutile IrO_2 and RuO_2 nanoparticles for oxygen evolution in acid and alkaline solutions. *J. Phys. Chem. Lett.* **2012**, *3*, 399−404.
(36) Pavlovic, Z.; Ranjan, C.; van Gastel, M.; Schlögl, R. The active site for the water oxidising anodic iridium oxide probed through in situ Raman spectroscopy. *Chem. Commun.* **2017**, *53*, 12414−12417.
(37) Pavlovic, Z.; Ranjan, C.; Gao, Q.; van Gastel, M.; Schlogl, R. Probing the structure of a water-oxidizing anodic iridium oxide catalyst using Raman spectroscopy. *ACS Catal.* **2016**, *6*, 8098−8105.
(38) Saeed, K. H.; Forster, M.; Li, J. F.; Hardwick, L. J.; Cowan, A. J. Water oxidation intermediates on iridium oxide electrodes probed by *in situ* electrochemical SHINERS. *Chem. Commun.* **2020**, *56*, 1129.
(39) Nong, H. N.; Falling, L. J.; Bergmann, A.; Klingenhof, M.; Tran, H. P.; Spori, C.; Mon, R.; Timshenko, J.; Zichittella, G.; Knop-Gericke, A.; Piccinin, S.; Perez-Ramirez, J.; Cuenya, B. R.; Schlogl, R.; Strasser, P.; Teschner, D.; Jones, T. E. Key role of chemistry versus bias in electrocatalytic oxygen evolution. *Nature* **2020**, *587*, 408−414.
(40) Nong, H. N.; Reiser, T.; Oh, H. S.; Gliech, M.; Paciok, P.; Vu, T. H. T.; Teschner, D.; Heggen, M.; Petkov, V.; Schlogl, R.; Jones, T.; Strasser, P. A unique oxygen ligand enviornment facilitates water oxidation in hole-doped $IrNiO_x$ core-shell electrocatalysts. *Nat. Catal.* **2018**, *1*, 841−851.
(41) Liao, P. C.; Chen, C. S.; Ho, W. S.; Huang, Y. S.; Tiong, K. K. Characterization of IrO_2 thin flims by Raman spectroscopy. *Thin Solid Films* **1997**, *301*, 7−11.
(42) Mo, Y.; Stefan, I. C.; Cai, W. B.; Dong, J.; Carey, P.; Sherson, D. A. In situ iridum L_{III}-edge x-ray absorption and surface enhanced raman spectroscopy of electrodepsited iridium oxide films in aqueous electrolytes. *J. Phys. Chem. B* **2002**, *106*, 3681−3686.
(43) Shan, J.; Zheng, Y.; Shi, B.; Davey, K.; Qian, S. Z. Regulating electrocatalysts via surface and interface enginerrting for acidic water electrooxidation. *ACS Energy Lett.* **2019**, *4*, 2719−2730.
(44) Montoya, J. H.; Seitz, L. C.; Chakthranont, P.; Vojvodic, A.; Jaramillo, T. F.; Norskov, J. K. Materials for solar fuels and chemicals. *Nat. Mater.* **2017**, *16*, 70−81.
(45) Siahrostrami, S.; Vojvodic, A. Influence of adsorbed water on the oxygen evolution reaction on oxides. *J. Phys. Chem. C* **2015**, *119* (2), 1032−1037.
(46) Zagalskaya, A.; Alexandrov, V. Role of defects in the interpaly between adsorbate evolving and lattice oxygen mechanisms of the oxygen evolution reaction in RuO_2 and IrO_2. *ACS Catal.* **2020**, *10*, 3650−3657.
(47) Shinagawa, T.; Garcia-Esparza, A. T.; Takanabe, K. Insight on Tafel slopes from a microkinetic analysis of aqueous electrocatalysis for energy conversion. *Sci. Rep.* **2015**, *5*, 13801 correction 2020, 10, 6899.

https://doi.org/10.1021/jacs.1c03473
J. Am. Chem. Soc. 2021, 143, 15616−15623